Journal of Luminescence 131 (2011) 342–346

Contents lists available at ScienceDirect

Journal of Luminescence

journal homepage: www.elsevier.com/locate/jlumin

Strong infrared-to-visible frequency upconversion in Er^{3+}-doped Sr_2CeO_4 powders

Nikifor Rakov [a,*], Renato B. Guimarães [b], Glauco S. Maciel [b]

[a] PG-Ciência dos Materiais, Universidade Federal do Vale do São Francisco, 48902-300 Juazeiro, BA, Brazil
[b] Instituto de Física, Universidade Federal Fluminense, 24210-346 Niterói, RJ, Brazil

ARTICLE INFO

Article history:
Received 19 May 2010
Received in revised form
21 October 2010
Accepted 26 October 2010
Available online 30 October 2010

Keywords:
Powder phosphors
Upconversion
Rare-earths

ABSTRACT

Efficient upconversion (UC) luminescence is demonstrated in Er^{3+}:Sr_2CeO_4 powders prepared by combustion synthesis and exposed to near-infrared (~975 nm) radiation. The UC emission lines observed at ~530, ~550 and ~665 nm correspond, respectively, to $^2H_{11/2}\rightarrow{}^4I_{15/2}$, $^4S_{3/2}\rightarrow{}^4I_{15/2}$ and $^4F_{9/2}\rightarrow{}^4I_{15/2}$ 4f–4f transitions of Er^{3+}. X-ray powder diffraction data showed that the $SrCO_3$ phase (impurity) is dramatically reduced when Sr^{2+} is partially substituted by Mg^{2+} ions. The UC phenomenon was investigated by use of continuous wave and pulsed laser excitation and the UC mechanism was attributed to energy transfer between excited Er^{3+} ions.

1. Introduction

Upconversion (UC) is the process in which infrared photons are converted into visible light and in rare-earth (RE) doped materials UC may occur via sequential multi-photon absorption. This optical process has found applications in photonics ranging from imaging to sensing and amplification [1–3]. The main characteristics of UC in RE doped materials is narrow emission bands and long lifetimes (up to some ms) owing to forced dipole electronic transitions inside 4f band. The most studied RE ion for UC production is erbium trivalent (Er^{3+}) because this RE ion has many 4f electronic states regularly spaced, which favors UC generation by use of a single monochromatic infrared source. As we move towards miniaturization, UC has been investigated in RE doped nanocrystalline structures. For example, up to four-photon induced UC (1.48–0.38 μm light conversion) has been observed in $Er_3Al_5O_{12}$ powders prepared by combustion synthesis [4].

Sr_2CeO_4 is a material that presents luminescence associated to a metal–ligand charge transfer. This process occurs between the lower coordination number terminal O atoms associated with the low-dimensional structure, in combination with an adjacent Ce^{4+} center in Sr_2CeO_4 structure [5]. The emission is fairly broad at the blue region (450–500 nm), which makes this material a potential candidate for phosphor applications. For example, Sr_2CeO_4 powders have been investigated for field emission display [6] and it has been demonstrated white luminescence when this powder was co-doped with trivalent rare-earth ions dysprosium and europium and excited by UV light [7]. In Ref. [8], the luminescence efficiency of Sr_2CeO_4 powders prepared by two different synthesis methods (sol–gel and solid state) and heat-treated at various temperatures was investigated using UV light as an excitation source. As far as we know, no report of UC luminescence was reported for Sr_2CeO_4 bulk or nanostructure. Here, we show the observation UC luminescence in Er^{3+} doped Sr_2CeO_4 crystalline powders prepared by combustion synthesis [9]. We also investigated the influence of Er^{3+} concentration on the UC emission profile of our powders.

2. Experimental section

Samples were prepared using combustion synthesis technique [9]. Reagent-grade of erbium nitrate [$Er(NO_3)_3\cdot 6\,H_2O$], strontium nitrate [$Sr(NO_3)_2$], cerium nitrate [$Ce(NO_3)_3\cdot 6\,H_2O$], magnesium nitrate [$Mg(NO_3)_2\cdot 6\,H_2O$] and urea (CH_4N_2O), with the purity of over 99.9%, were used as raw materials. The metal nitrates and urea were mixed, in an appropriate molar ratio, in a minimum amount of de-ionized water. The mixed solution was then kept under constant stirring, at room temperature, to transform into a transparent viscous gel. Afterward, the resultant gel was put in a porcelain crucible and it was placed in a furnace preheated to 500 °C, until excess free water evaporated and spontaneous ignition occurred, resulting in fine powder product, which was grounded and sintered at 1200 °C for 2 h in an air atmosphere with a heating rate of 400 °C/h and a cooling rate of 400 °C/h.

* Corresponding author.
E-mail address: nikifor.gomez@univasf.edu.br (N. Rakov).

0022-2313
doi:10.1016/j.jlumin.2010.10.034

The crystalline structure of the powders was analyzed by X-ray powder diffraction (XRPD). The diffractometer used was a Bruker AXS D8 Advance with a Cu target ($K_{\alpha1\alpha2}$ radiation of 40 kV and 40 mA) and operation in a Bragg–Brentano θ/θ configuration. The diffraction patterns were collected in a flat geometry with steps of 0.02 degrees and an accumulation time of 30 s per step.

For optical analysis, the fresh powders were pressed and held fixed between two microscope slides that were used as sample holder. The estimated powder thickness was ~0.5 mm. The UC measurements were performed using a continuous wave (cw) diode laser operating at $\lambda \sim 975$ nm and a Nd:YAG Q-Switched pumped tunable OPO (5 ns, 10 Hz) as the excitation sources. The laser was focused on the input sample face (spot size of ~1 mm) by use of a 10 cm focal length lens. The maximum laser power at the sample surface was ~500 mW. The UC luminescence was collected by an optical fiber attached to the output window of the sample holder and sent to a compact spectrometer. The laser light at the output window of the sample holder was rejected by use of a cut-off optical filter. All measurements were performed at room temperature.

3. Results and discussion

Fig. 1 shows the XRPD data for one of the samples studied in this work. The crystalline phases were identified with the International Centre for Diffraction Data (ICDD) database and the XRPD data were refined following the Rietveld method with the GSAS software [10] using EXPGUI graphical interface [11]. The fitting is quite satisfactory as can be observed in the inset, which displays a zoomed region of the spectrum. The other samples studied here present the same fitting quality. Table 1 shows the phases that have been identified in each investigated sample. In samples containing Sr^{2+} and Mg^{2+} we assumed that both ions form isostructural lattices and the diffraction planes were indexed using database of phases containing Sr, Ce and O. Our results show that in addition to the Sr_2CeO_4 phase it is possible to detect the presence of "impurity" phases, more specifically, $SrCO_3$, CeO_2 and $SrCeO_3$. The presence of these phases indicates that the heat treatment temperature and time were not sufficient to eliminate all the impurities [12]. In Table 1 it is shown that the presence of Mg^{2+} in our samples drastically reduced the amount of $SrCO_3$. The presence of carbon in $SrCO_3$ phase would increase the phonon cut-off energy and as a consequence it would produce a quenching of Er^{3+} luminescence in such an environment. While the dominant phase is Sr_2CeO_4 it is not possible to infer which is the location of Er^{3+} in our samples based on XRPD data. The valence of erbium (+3) is different from that of strontium (2+) and cerium (4+) in the phases detected here and therefore it appears that erbium cannot replace one of these ions into the sublattice. Nevertheless, luminescence from trivalent RE ions has been observed in crystalline hosts containing Ca^{2+} and Zr^{4+} and the replacement of these ions by trivalent REs is obtained via charge compensated sites [13,14]. Table 1 also shows that the substitution of Sr^{2+} by Mg^{2+} reduced the lattice parameters. This is reasonable as Mg^{2+} has a smaller radius than Sr^{2+} (0.65 Å compared with 1.13 Å). The substitution of Sr^{2+} by Mg^{2+} cannot destroy the local structure around the rare-earth ions, but only modifies the local symmetry around Er^{3+}. Smaller cell volumes would imply in reduced spatial separation between Er^{3+} ions and therefore the presence of Mg^{2+} may improve electronic interactions among neighboring Er^{3+} ions and enhance UC luminescence produced via energy transfer mechanisms. Fig. 2(a) shows the UC emission spectra of $[Sr_{0.7}Mg_{0.3}]_2CeO_4$ powder containing Er^{3+} (as-prepared concentrations of 0.5, 1.0, 2.0 and 4.0 wt%) and exposed to cw laser excitation at $\lambda \sim 975$ nm. The samples present three bands centered at ~530, ~550 and ~665 nm corresponding, respectively, to $^2H_{11/2} \rightarrow {}^4I_{15/2}$, $^4S_{3/2} \rightarrow {}^4I_{15/2}$ and $^4F_{9/2} \rightarrow {}^4I_{15/2}$ 4f–4f excited state to ground state transitions of Er^{3+}. Note that the red emission band increases with Er^{3+} concentration. As a consequence, the green-to-red intensity ratio decreases with the increase of Er^{3+} concentration as shown in Fig. 2(b). Fig. 3 shows the UC spectrum of $[Sr_{0.7}Mg_{0.3}]_2CeO_4$ powder doped with 4.0 wt% of Er^{3+} and exposed to pulsed (5 ns) laser excitation at $\lambda \sim 975$ nm. Note that the red emission band is very weak, which differs from what was presented in Fig. 2(a) when the same sample was irradiated with cw laser light.

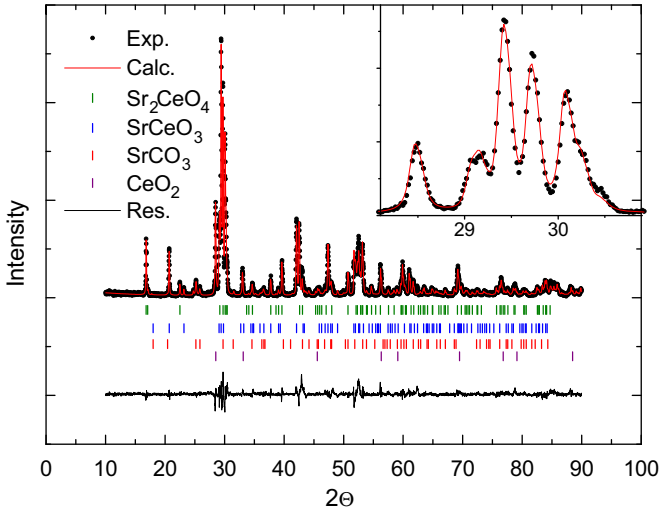

Fig. 1. XRPD data for one of the samples studied in this work. The sample is $[Sr_{0.7}Mg_{0.3}]_2CeO_4$ powder.

The behavior shown in Fig. 2(a) and (b) are associated to Er^{3+} concentration dependent processes such as energy transfer between neighboring erbium ions. The most relevant excitation channels and relaxation pathways proposed are shown in Fig. 4. The UC emission is produced as follows: first, laser induced ground-state absorption (GSA) takes place populating excited state $^4I_{11/2}$ of Er^{3+} (upward solid arrow, Fig. 4) followed by excited state absorption (ESA) from level $^4I_{11/2}$ to level $^4F_{7/2}$ (upward solid arrow, Fig. 4). As the doping concentration increases, dipole–dipole energy transfer mechanisms between nearby Er^{3+} ions become more efficient than ESA [1]. In this case, the energy transfer mechanism promotes one Er^{3+} ion populated at $^4I_{11/2}$ to the higher lying level $^4F_{7/2}$ while a neighboring Er^{3+} ion also populated at $^4I_{11/2}$ is taken back to the ground state (dotted lines labeled as "I" in Fig. 4). After nonradiative relaxation (downward wigged arrow) from level $^4F_{7/2}$ to levels $^2H_{11/2}$ and $^4S_{3/2}$, green UC emission follows. Channel "I" is more effective under cw excitation as pulsed excitation would promote the instantaneous GSA+ESA transition $^4I_{15/2} \rightarrow {}^4I_{11/2} \rightarrow {}^4F_{7/2}$ and in this case there would not be enough population at intermediate state $^4I_{11/2}$ to generate the energy transfer process "I". The red UC emission may follow two excitation pathways: (a) after population reaches level $^4S_{3/2}$, it decays nonradiatively to the red emitting level $^4F_{9/2}$; (b) after ground-state absorption ($^4I_{15/2} \rightarrow {}^4I_{11/2}$), the population at level $^4I_{11/2}$ decays nonradiatively to level $^4I_{13/2}$ and a second absorption step (ESA) populates the red emitting level $^4F_{9/2}$. Generally this is an off-resonant excitation mechanism and therefore it is very unlikely to occur. The decrease of the green-to-red intensity ratio shown in Fig. 2(b) indicates that an Er^{3+} concentration dependent process is present. These observations may be explained if one considers the presence of a cross-relaxation channel (dotted lines labeled as "II" in Fig. 4). Channel "II" involves populating $^4F_{9/2}$ level by bypassing the green emission level [15]. This mechanism involves one Er^{3+} ion populated at $^4F_{7/2}$, which decays to level $^4F_{9/2}$ while promoting an excited neighboring

Table 1
Structural parameters obtained from the XRPD data of the oxide powders studied in this work.

Sample	Phase symmetry space group	Weight fraction (%)	Lattice parameters (Å)	PDF code
Sr_2CeO_4	Sr_2CeO_4		$a=6.115880$	
	Orthorhombic	31.5	$b=10.342592$	089-5546
	Pbam		$c=3.595459$	
	$SrCeO_3$		$a=6.005295$	
	Orthorhombic	19.3	$b=6.142700$	082-2427
	Pbnm		$c=8.575834$	
	CeO_2		$a=5.424508$	
	Cubic	8.4	$b=5.424508$	043-1002
	Fm-3m		$c=5.424508$	
	$SrCO_3$		$a=5.101337$	
	Orthorhombic	40.8	$b=8.412442$	071-2393
	Pmcn		$c=6.023513$	
Er:Sr_2CeO_4	Sr_2CeO_4		$a=6.112331$	
	Orthorhombic	43.4	$b=10.342176$	089-5546
	Pbam		$c=3.592522$	
	$SrCeO_3$		$a=6.138845$	
	Orthorhombic	14.5	$b=6.000138$	082-2427
	Pbnm		$c=8.573315$	
	CeO_2		$a=5.421906$	
	Cubic	1.8	$b=5.421906$	043-1002
	Fm-3m		$c=5.421906$	
	$SrCO_3$		$a=5.093694$	
	Orthorhombic	40.3	$b=8.420245$	071-2393
	Pmcn		$c=6.022620$	
$[Sr_{0.7}Mg_{0.3}]_2CeO_4$	Sr_2CeO_4		$a=6.115342$	
	Orthorhombic	47.9	$b=10.350014$	089-5546
	Pbam		$c=3.594963$	
	$SrCeO_3$		$a=6.140917$	
	Orthorhombic	33.2	$b=6.008701$	082–2427
	Pbnm		$c=8.578268$	
	CeO_2		$a=5.424705$	
	Cubic	11.2	$b=5.424705$	043-1002
	Fm-3m		$c=5.424705$	
	$SrCO_3$		$a=5.102041$	
	Orthorhombic	7.7	$b=8.410407$	071-2393
	Pmcn		$c=6.019967$	
Er:$[Sr_{0.7}Mg_{0.3}]_2CeO_4$	Sr_2CeO_4		$a=6.110408$	
	Orthorhombic	48.9	$b=10.342693$	089-5546
	Pbam		$c=3.591830$	
	$SrCeO_3$		$a=6.135972$	
	Orthorhombic	30.9	$b=6.000499$	082-2427
	Pbnm		$c=8.571856$	
	CeO_2		$a=5.420903$	
	Cubic	5.9	$b=5.419447$	043-1002
	Fm-3m		$c=5.419447$	
	$SrCO_3$		$a=5.067770$	
	Orthorhombic	14.3	$b=8.477072$	071-2393
	Pmcn		$c=6.027364$	

Er^{3+} ion populated at level $^4I_{11/2}$ to the higher lying level $^4F_{9/2}$. Channel "II" would be active in both cw and pulsed excitation but we can see from Figs. 2(a) and 3 that the UC emission profiles of the same sample ($[Sr_{0.7}Mg_{0.3}]_2CeO_4$ powder doped with 4.0 wt% of Er^{3+}) are quite different. This is an indication that under cw excitation the red emission is not (mainly) generated by the route that produces the green emission (the pathway that involves populating $^4F_{7/2}$). Instead, the red emission must follow the independent pathway that involves the energy transfer channel labeled as "III" in Fig. 4. In this case, after nonradiative decay from level $^4I_{11/2}$ to level $^4I_{13/2}$, one Er^{3+} ion interacts with another excited neighboring Er^{3+} ion (still populated at $^4I_{11/2}$) and energy transfer takes place promoting one ion to $^4F_{9/2}$ state while the other ion returns to the ground state (see Fig. 4). Therefore channel "III" must be efficient only under cw excitation when continuous loading of states $^4I_{11/2}$ and $^4I_{13/2}$ is available in order to keep this energy transfer channel opened.

We are left with the issue of which is the phase responsible for the UC luminescence. We tested our samples under UV excitation. Fig. 5 shows the emission spectra of two of our samples under xenon lamp illumination (excitation at $\lambda=256$ nm). Note that the characteristic blue emission from the host (luminescent associated to a metal–ligand charge transfer) is strongly quenched in the sample containing Er^{3+} while the characteristic green and red emissions from Er^{3+} is clearly observed. In this case, it is possible to speculate about the origin of the quenching process. The main phases observed in our samples are $SrCeO_3$ and Sr_2CeO_4 but the $SrCeO_3$ phase is not luminescent [5] and therefore we must consider that the host-to-Er^{3+} energy transfer must be occurring in the Sr_2CeO_4 phase. Hirai and Kawamura [16] observed host-to-Er^{3+} energy transfer from the triplet excited state of the metal–ligand charge transfer state in Er^{3+}:Sr_2CeO_4 when the sample was excited by UV light and we believe that the same effect is occurring in our powders.

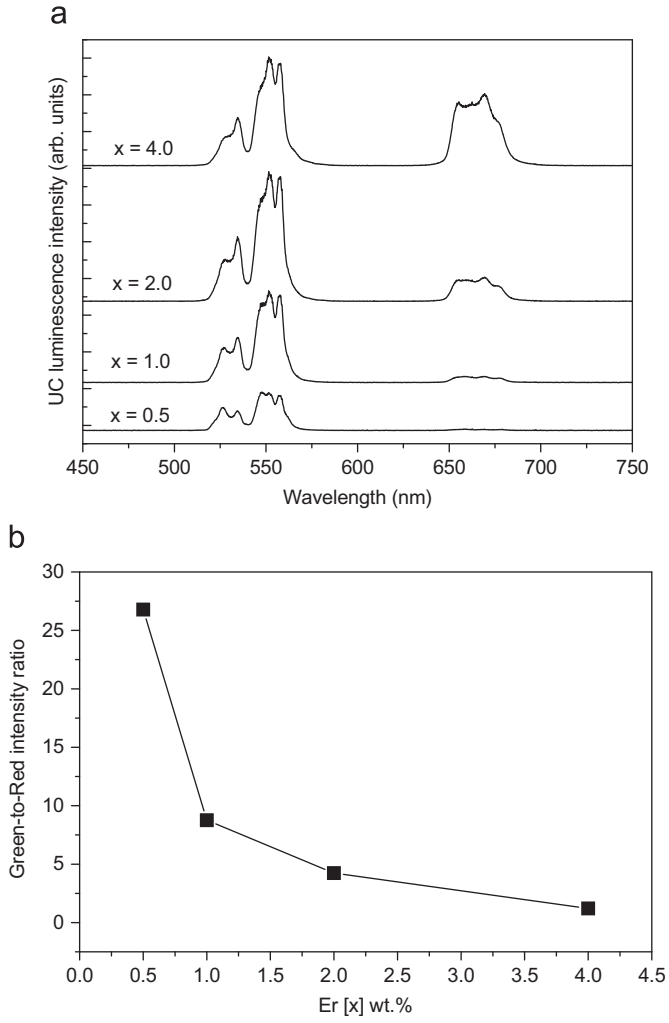

Fig. 2. (a) UC emission spectra of Er:$[Sr_{0.7}Mg_{0.3}]_2CeO_4$ powders containing different Er^{3+}wt% concentrations under cw near-infrared excitation. (b) Green-to-red intensity ratio for the samples studied in this work. Laser excitation wavelength: 975 nm; excitation power: 500 mW.

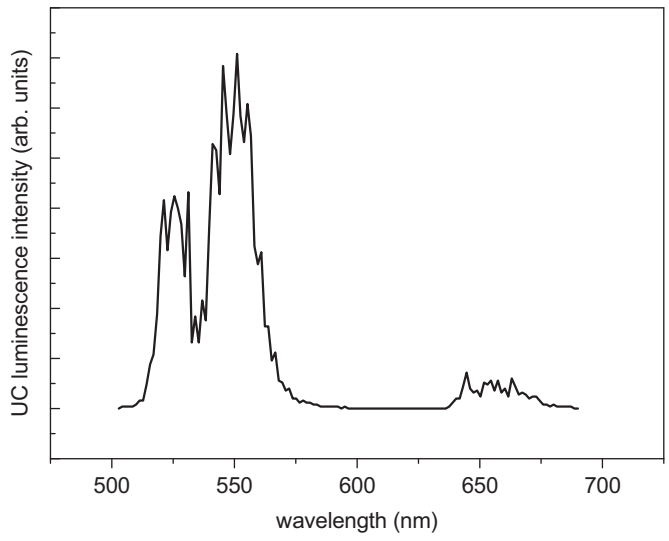

Fig. 3. (a) UC emission spectrum of Er:$[Sr_{0.7}Mg_{0.3}]_2CeO_4$ powder containing 4.0 wt% of Er^{3+} under pulsed laser excitation. Laser characteristics: excitation wavelength of 975 nm; pulse duration of 5 ns; repetition rate of 10 Hz.

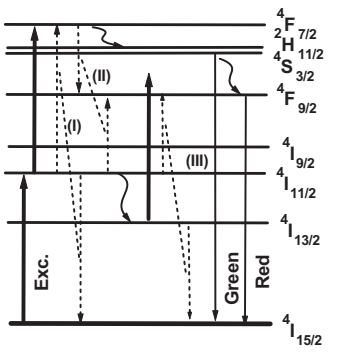

Fig. 4. Energy levels diagram of Er^{3+} with detailed UC mechanisms.

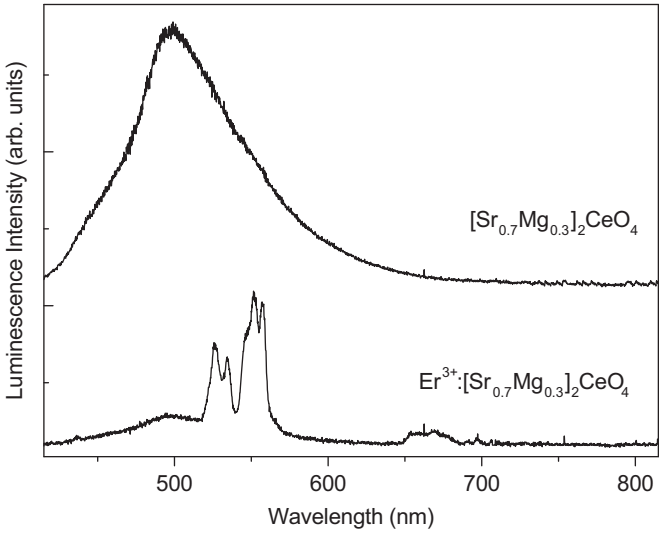

Fig. 5. Luminescence under UV lamp excitation (λ=256 nm) for $[Sr_{0.7}Mg_{0.3}]_2CeO_4$ powder undoped and doped with 4.0 wt% of Er^{3+}.

4. Conclusions

Infrared-to-visible frequency UC emission was observed in Er^{3+} doped Sr_2CeO_4 powders prepared by combustion synthesis. The XRPD analysis showed the presence of "impurity" phases, more specifically, $SrCO_3$, CeO_2 and $SrCeO_3$ which were not eliminated during the heat treatment. The XRPD data also showed that the impurity phase $SrCO_4$ was drastically reduced by partially replacing Sr^{2+} by Mg^{2+}. The UC luminescence also indicated the presence of Er–Er energy transfer mechanisms and under UV excitation the characteristic blue emission of the Sr_2CeO_4 phase was quenched in favor of the green and red emissions of Er^{3+} ions indicating that erbium must be close to cerium ions in the host-to-Er^{3+} energy transfer.

Acknowledgements

This work was partially supported by the Brazilian Agency Conselho Nacional de Desenvolvimento Científico e Tecnológico (CNPq). One of the authors (N. Rakov) acknowledges financial support from FAPESB.

References

[1] F. Auzel, Chem. Rev. 104 (2004) 139.
[2] P.N. Prasad, Nanophotonics, Wiley, New York, 2004.

[3] J. Evans-Freeman, P. Goldner, T. Kimura, P. Ruterana (Eds.), The Proceedings of the European Materials Research Society 2007, Symposium C: Rare Earth Ion Doping for Photonics: Materials, Mechanisms and Devices, Mater. Sci. Eng. 146 2008 1.
[4] G.S. Maciel, N. Rakov, M. Fokine, I.C.S. Carvalho, C.B. Pinheiro, Appl. Phys. Lett. 89 (2006) 081109.
[5] E. Danielson, M. Devenney, D.M. Giaquinta, J.H. Golden, R.C. Haushalter, E.W. McFarland, D.M. Poojary, C.M. Reaves, W.H. Weinberg, X.D. Wu, Science 279 (1998) 837.
[6] Y.D. Jiang, F. Zhang, C.J. Summers, Z.L. Wang, Appl. Phys. Lett. 74 (1999) 1677.
[7] T. Hirai, Y. Kawamura, J. Phys. Chem. B. 109 (2005) 10569.
[8] C.H. Lu, C.T. Chen, J. Sol–gel Sci. Technol. 43 (2007) 179.
[9] N. Rakov, F.E. Ramos, G. Hirata, M. Xiao, Appl. Phys. Lett. 83 (2003) 272.
[10] A.C. Larson, R.B. Von Dreele, General structure analysis system (GSAS), Los Alamos National Laboratory Report LAUR (1994) 86–748.
[11] B.H. Toby, J. Appl. Cryst. 34 (2001) 210.
[12] J. Gomes, A.M. Pires, O.A. Serra, Quim. Nova 27 (2004) 706.
[13] D.R. Tallant, J.C. Wright, J. Chem. Phys. 63 (1975) 2074.
[14] D. van der Voort, G. Blasse, Chem. Mater. 3 (1991) 1041.
[15] F. Vetrone, J.C. Boyer, J.A. Capobianco, A. Speghini, M. Bettinelli, Chem. Mater. 15 (2003) 2737.
[16] T. Hirai, Y. Kawamura, J. Phys. Chem. B. 108 (2004) 12763.